Development of high gradient quadrupole magnets in HEPS storage ring

Mei Yang,[*] Yingshun Zhu,[*,†] Yafeng Wu, Xianjing Sun, Qing Li, Ran Liang, Chuang Shen, Siyu Chen, Yuandi Xu, Shu Yang, Lei Wu,[*] Chunhua Li,[*] Yi Jiao,[*] and Fusan Chen[*,‡]

Institute of High Energy Physics, Chinese Academy of Sciences, Beijing 100049, China

(Received 25 September 2025; accepted 16 July 2026; published 12 August 2026)

The High Energy Photon Source is the first fourth-generation light source in China, featuring a hybrid multibend achromat lattice. This innovative design incorporates high gradient quadrupoles with an aperture of 26 mm, a gradient of about 80 T/m, and high-order field harmonics of less than 4×10^{-4}. This paper details the optimized magnetic design, precise fabrication techniques, batch field measurements, and a method for field harmonic compensation utilizing a magic finger. A comparative analysis was conducted on nine types of the 480 pure quadrupole magnets that share the same cross section but differ in iron lengths. These variations include laminated or solid cores and closed or open yokes. The cross section, characterized by a narrow concave and convex pole contour, a tapered pole root, and saddle coils, is designed to mitigate magnetic saturation while enhancing the iron filling ratio. The impact of iron saturation on the transfer function and the evolution of current-dependent multipole fields has been systematically investigated, along with the effects of mechanical errors and inhomogeneities in the magnetic properties of the iron core on harmonics. We demonstrate a comprehensive engineering solution for high gradient small-aperture quadrupole magnets, which has been validated through mass production.

DOI: 10.1103/cg6l-1z6m

I. INTRODUCTION

The High Energy Photon Source (HEPS) is the first fourth-generation synchrotron light source under construction in China. Its accelerator complex contains a 6 GeV storage ring, a full energy booster, a 500 MeV linac, and three transport lines [1].

The storage ring of HEPS is 1.36 km in circumference and has an ultralow natural emittance of less than 40 pm rad. Such an ultralow emittance is achieved by increasing the number of dipole magnets and employing strong transverse focusing. The HEPS storage ring comprises 48 seven-bend achromat (7BA) cells that are grouped in 24 superperiods [2]. As shown in Fig. 1, there are 37 magnets in one cell: 5 longitudinal gradient dipoles [3], 14 high gradient quadrupoles, 6 combined dipoles and quadrupoles, 6 sextupoles, 2 octupoles [4], and 4 fast correctors. The dipole magnets are permanent magnets, and the others are electromagnets. All the magnets have small apertures and are compact to reduce the size of the electron beam compared with the magnets used in third-generation light sources.

The achievement of a compact multibend achromat (MBA) lattice possessing strong transverse focusing necessitates the use of high gradient quadrupoles, operating at gradients of about 50 to 100 T/m. Thus, the magnet aperture is reduced from typically 70 to about 25 mm, as reported in several light sources, such as ESRF-EBS [5], APS-U [6], and MAX IV [7].

The HEPS quadrupoles operate at a nominal gradient of about 80 T/m with a 26 mm aperture. The magnet aperture is mainly governed by the 24 mm outer diameter of the vacuum chamber and its installation tolerance. Within each 7BA cell, the 14 quadrupoles are divided into three families: standard type I, type II (with stainless steel supporter for x-ray ports, seen in Fig. 2), and type I with additional windings allowing horizontal and vertical dipole corrections. This study concentrates mainly on the design and field performance of pure quadrupoles, i.e., type I and type II quadrupoles.

To facilitate mass production, all 480 pure quadrupole magnets are designed with the same pole profile and similar cross section while varying in iron length, ranging from 180 to 327 mm. Consequently, both laminated and

[*]Also at University of Chinese Academy of Sciences, Beijing, China.
[†]Contact author: yszhu@ihep.ac.cn
[‡]Contact author: chenfs@ihep.ac.cn

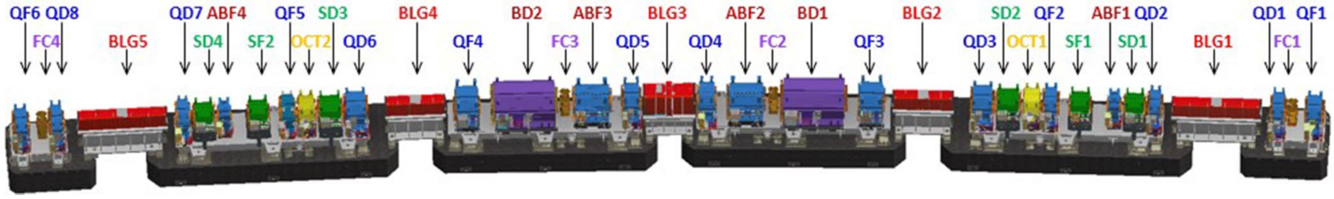

FIG. 1. Layout of one arc cell (1/48) of the HEPS storage ring lattice. BLG: longitudinal gradient dipoles; QD, QF: quadrupoles; ABF, BD: combined dipole and quadrupole magnets; SD, SF: sextupoles; OCT: octupoles; FC: fast correctors.

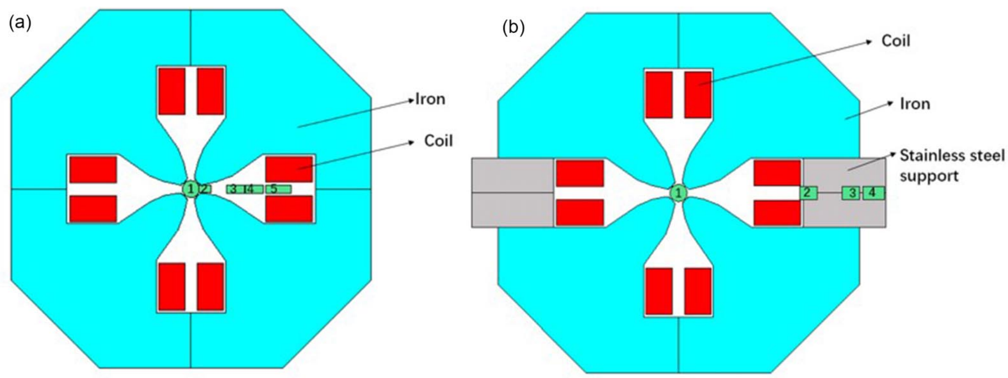

FIG. 2. Cross section of type I (a) and type II (b) quadrupole with circulating beam vacuum chamber (region 1) and x-ray extraction ports (region 2, 3, 4, or 5).

solid magnets are available to accommodate different manufacturers' expertise and cost considerations. The high magnetic field gradient and strict field quality requirements present significant challenges for the batch production of these quadrupole magnets.

The magnet design is detailed in Sec. II, including the overall considerations, type I/II comparative analysis, pole root angle optimization, error tolerance studies, and a field compensation method. Section III delineates the mechanical design and manufacturing process. The challenges encountered during the initial production phase, along with their resolutions and analysis, are detailed in Sec. IV. Finally, Sec. V presents statistical analysis of field measurement results for batch quadrupole magnets.

II. MAGNET DESIGN

A. Design considerations and criteria of quadrupoles in HEPS

The magnet specifications are stringent, as detailed in Table I. Multipole components are expressed in units of 10^{-4} relative to the main quadrupole field at a reference radius of 5 mm. The normal and skew components of 2n-pole are presented as b_n and a_n, respectively.

TABLE I. Main requirements of the pure quadrupoles in the HEPS storage ring.

Type	Units	(QF1/6)[a]	(QF2/5)[b]	(QD2/7)[b]	(QD3/6)[c]	(QD4/5)[b]
Quantity	/	48/48	48/48	48/48	48/48	48/48
Field gradient	T/m	78.21	79.52	77.76	78.05	77.07
Bore diameter	mm	26	26	26	26	26
Iron length	mm	201/245	201	180	327	260
Good field region radius	mm	5	5	5	5	5
Harmonics—b_3, a_3[d]	1×10^{-4}	<4	<4	<4	<4	<4
Harmonics—b_4, a_4	1×10^{-4}	<4	<4	<4	<4	<4
Harmonics—b_5, a_5	1×10^{-4}	<2	<2	<2	<2	<2
Harmonics—b_n, a_n $(n>5)$	1×10^{-4}	<1	<1	<1	<1	<1

[a]QF1 and QF6 are different in odd and even 7BA cells.
[b]QF5, QD4, and QD7 are type II quadrupoles.
[c]QD3 and QD6 are the same and are called QD36.
[d]b_3 and a_3 indicate normal and skew sextupole field components, respectively.

The magnets must satisfy the following constraints and boundary conditions [8]:

(1) Field performance: Quadrupoles have to provide a high gradient (~80 T/m nominal) while maintaining field quality specified in Table I. The high-field gradient for all quadrupoles minimizes the longitudinal space of magnets in HEPS arc regions, accommodating auxiliary components (beam position monitors and vacuum chamber bellows) and ensuring sufficient iron separations to reduce field crosstalk effects. The crosstalk effects between adjacent magnets were systematically incorporated into the lattice modification, based on detailed field simulations [9,10].

(2) Vacuum integration: Boundary conditions include a dual vacuum system in scheduled 90 beam lines, which have x-ray ports extracted from insertion devices (IDs) and dipole magnets (BLG3s). These occupy distinct transverse positions between adjacent coil packages (> 13 mm clearance), interpole gaps (≥ 11 mm), and yoke horizontal planes. The type II quadrupoles (QD4, QF5, and QD7) incorporate stainless steel supporters with horizontal perforations for x-ray ports.

(3) Secondary constraints: Design optimization prioritizes low power consumption (achieved through current density management), minimal temperature rise, controlled coolant flow velocity (< 2 m/s), and manufacturability.

B. Magnet design of high gradient quadrupole

The magnetic field simulation and optimization were performed using OPERA-2D/ST and OPERA-3D/TOSCA [11]. While a wider pole improves field quality within a specified good field region, the initial design features a smooth hyperbolic pole profile with 9 mm interpole gaps, exceeding boundary constraints imposed by the x-ray extraction vacuum chamber.

To accommodate the required 11 mm pole gap, an optimized pole profile was developed, as illustrated in Fig. 3 [8]. This profile features a central hyperbolic section, seamlessly transitioning into concave and convex arc shims. The contour is free of sharp discontinuities, ensuring manufacturability via machining or punching. At the end of the contour, a small platform (several millimeters in length) facilitates mechanical measurement and alignment. Beyond this platform, the pole expands progressively through three distinct opening angles: 11°, 22°, and 35°, relative to the horizontal axis, which effectively mitigates flux saturation in the lower pole.

Excitation coils for moderate gradient quadrupoles typically employ racetrack-shaped windings due to their straightforward winding process. However, high gradient quadrupoles necessitate tapered pole roots and correspondingly shaped coils. Figure 4 illustrates the pole root taper

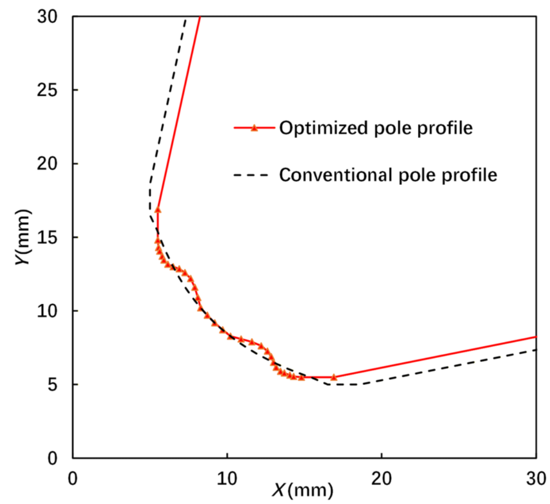

FIG. 3. The pole profile of a quadrupole in HEPS. Conventional pole profile (black dashed line) and optimized profile with 11 mm gap (red solid line).

angles of 0° and 45°, revealing a significantly expanded high-field region in the 45° configuration. The taper angle refers to the angle between the edge of the magnet pole at the coil position and the horizontal plane, as marked by θ in Fig. 4(b).

To systematically evaluate upper pole taper angle effects, we conducted simulations across a range of 0 to 45° in 5° increments while maintaining constant quadrupole external dimensions and Ampère-turns. As Fig. 5 shows, the central field gradient decreases monotonically with increasing taper angle. Notably, the 0° taper (accommodating saddle coils) provides the largest field gradient and superior mechanical integrity. This design minimizes pole deformation and enhances field reproducibility after magnet reassembly.

The iron saturation is even worse in the 3D simulation. At the operation current (Iop), the short length to aperture ratio and the end effect amplify the iron saturation. Figure 6 plots the calculated integral transfer function of QF16-201 as a function of current at the two pole taper

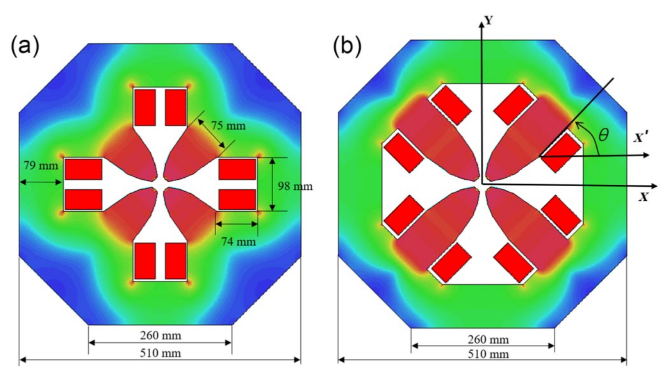

FIG. 4. Comparative flux density distributions in a quadrupole with a pole root taper angle $\theta = 0°$ (a) and $\theta = 45°$ (b).

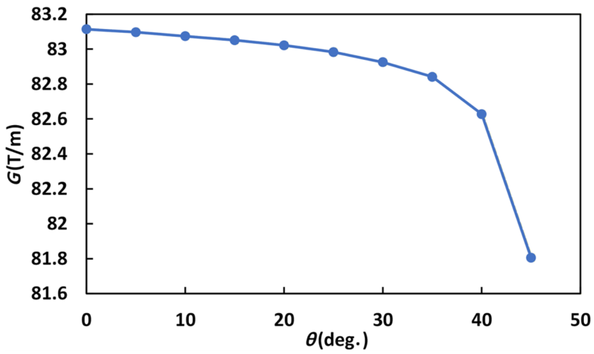

FIG. 5. Gradient versus pole root taper angle.

angles: 0° and 45°. The excitation efficiency (defined as $(\mathrm{GL/I})/(\mathrm{GL/I})_{0.2\,\mathrm{Iop}}$ drops sharply when the current exceeds 0.8 Iop. At Iop, the excitation efficiency is 92.9% for the saddle coils (pole root taper angle = 0°) and 89.3% for the racetrack coils (pole root taper angle = 45°). This 3.6% efficiency difference corresponds to a 4.25% higher integral gradient in the 0° configuration, confirming the 0° pole taper angle and saddle coil's superior saturation mitigation capability.

In the HEPS storage ring, all nine types of quadrupole magnets are designed with a 0° tapered pole root and saddle coil configuration. This design achieves a higher iron filling factor compared to configurations featuring other taper angles while maintaining identical magnet envelopes measuring 510 × 510 mm.

The coil width is constrained by the longitudinal end space requirements. To minimize power consumption [6], a low current density is selected. The conductor cross section is optimized to limit temperature rise. Active cooling is implemented with a water flow velocity of less than 2 mm/s to mitigate flow-induced vibrations, which could otherwise compromise field stability.

All quadrupole magnets employ a standardized $8 \times 8\ \mathrm{mm}^2$ copper conductor with a 3 mm diameter cooling

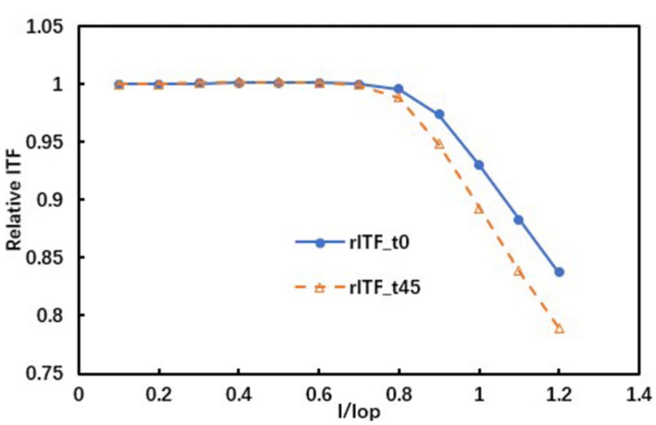

FIG. 6. Relative integral transfer function versus current in QF16-201.

TABLE II. Electrical and cooling parameters of the QD4/5 (Iron length = 260 mm).

Parameter	Units	QD4/5
Number of turns per pole	/	28
Excitation current	A	193
Conductor layers	/	4
Conductor cross section	mm	8 × 8
Cooling pipe diameter	mm	3
Current density	$\mathrm{A/mm^2}$	3.4
Magnet resistance	mΩ	38
Magnet inductance	H	0.016
Magnet power	kW	1.4
Pressure drops	$\mathrm{kg/cm^2}$	6
Number of cooling circuits	/	4
Cooling water speed	m/s	1.72
Temperature rise	°C	7

hole, except for the longest magnet (QD36), which features a 4 mm cooling hole to cut down its temperature rise. The maximum temperature rise of nine types of magnets does not exceed 8 °C. As an example, the electrical and cooling parameters of QD4/5 are listed in Table II.

The integrated magnetic field characteristics were simulated using OPERA/3D. For short quadrupoles with iron length below 201 mm, the integrated multipoles less than 0.6×10^{-4} are realized by a 60° end chamfer with a 2 mm depth, which mitigates the systematic harmonics caused by end effect, especially the b_6. Longer quadrupoles do not need an end chamfer, as the pole shim profiles compensate for the end effect.

Simulation results demonstrate excellent harmonic suppression across all nine quadrupole types, with symmetric multipoles constrained to less than 0.6 units at their nominal gradient. Field optimization was performed across an 80%–105% tuning range of the nominal gradient (about 80 T/m), with iron saturation-induced multipole variations maintained within an acceptable range. Taking the symmetry model of QD36 simulation, for instance, the b_6 component decreases from −0.21 units to −0.55 units as the exciting current is tuned from 80% to 105% of its rated value.

C. Comparative field distribution in type I and type II quadrupole

The type I and type II quadrupoles share an identical cross section, with the exception of stainless steel plates at the horizontal plane in type II quadrupoles. As shown in Fig. 7, 2D simulations under identical Ampère-turns reveal significant differences in field distribution. The field in the center of the upper yoke reaches 1.44 T inthe type II quadrupole and is almost twice that of the type I quadrupole with a field strength of 0.73 T, corresponding to a gradient of 78.86 T/m in type II and 79.27 T/m in type I. Type II magnets are more saturated with the same cross

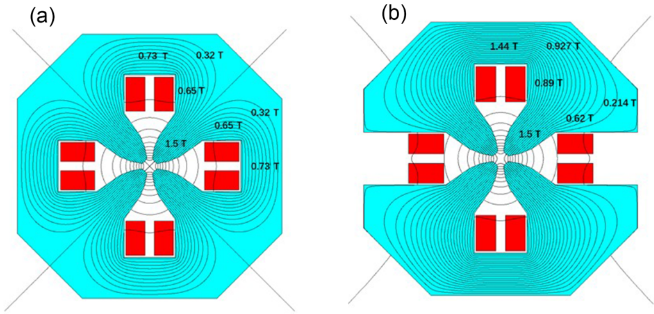

FIG. 7. Flux distribution and B_{mod} in type I (a) and type II (b) quadrupoles.

section and magnetic material. Due to stainless steel's small relative permeability ($\mu_r \approx 1$) compared to the laminated steel ($\mu_r > 4000$), the magnetic flux passes through the upper yoke with a small magnetic resistance in the type II quadrupole. Despite this, both the excitation coils and pole configuration preserve the quadrupole symmetry, which complies with the stringent field quality requirements for high-performance applications.

D. Field error analysis

Even though the magnet design can theoretically meet the requirements on paper, in reality, the fabrication tolerances, assembly errors of the magnet, the uncertainties about the magnetic properties of the iron, and other imponderables make it difficult to obtain the designed specifications. Based on error calculations of magnetic fields and previous magnet manufacturing experience, the main focus was placed on machining and assembly errors.

The disturbance of magnetic field harmonics caused by random position errors of the pole surface with a maximum deviation of 0.01 mm is mainly the sextupole component, with a typical value of about 1.0×10^{-4}. When the gradient is lower, the induced harmonics will be larger. In a typical case where the pole is moved by 0.01 mm relative to its ideal position, the assembly errors of the four quadrants can cause a maximum sextupole term of about 3.6×10^{-4}. For the type II quadrupole, if the relative magnetic permeability of stainless steel on the horizontal plane is 1.2, the induced extra harmonics are about 0.1×10^{-4}.

The material properties are also taken into consideration. Local regions of the pole with a 3% difference in BH curves are set; then the induced typical sextupole component is 1.3×10^{-4} for the pole tip region and 0.7×10^{-4} for the pole root region.

Manufacturing costs correlate directly with mechanical tolerances and assembly complexity. With the error analysis, key technological specifications are established for batch production. The deviations of the magnet-inscribed circle should be better than ± 0.02 mm for solid iron and ± 0.03 mm for laminated iron, and the clearance between adjacent poles shall be held to the same specifications. The BH curves of DT4 solid iron or silicon steel sheets must not be lower than the specified values. The stacking factor of punched laminations is at least 98%.

E. Field compensation method

As the field quality requirements for batch production are stringent, it is difficult to control the fabrication tolerances and material properties due to the mechanical limitations and a tight schedule. The magic finger technique is used to compensate for high-order nonsystem field harmonics that exceed the design requirement, such as the sextupole and octupole components in quadrupole magnets [12].

The magic finger used for HEPS quadrupoles is a slender rectangular block made of solid pure iron, with dimensions of 11 mm width, 8 mm thickness, and 38 mm length. It can be installed at the magnet pole end in slots on the connecting plate between the upper two poles or the lower two poles, with its symmetrical center line passing through the center of the aperture. A screw is used to press it tightly against the pole end.

When a quadrupole magnet is energized, the magnetization of the finger generates a magnetic field, while the presence of the finger alters the magnetization in the surrounding regions of the iron poles. Together, these two parts produce an extra magnetic field, with the ratio of normal to skew components varying according to the angle of the magic finger. Furthermore, the amplitude of the generated harmonic components depends critically on the finger's dimension and material properties, the radial distance from the quadrupole aperture center, the quadrupole's integral field strength, and the saturation level. As the harmonic order increases, the magic finger's adjustability declines exponentially. For HEPS quadrupole magnets, the fingers are arranged at integer multiple angles of 22.5°, which enables the largest possible octupole component adjustment.

There are upper and lower pole connecting plates at both ends of the magnet. As illustrated in Fig. 8, there exist four magic finger slots on a pole head connecting plate, thus yielding a total of 16 slots in a magnet. The angles corresponding to these slots at each end are $\pi/8$, $3\pi/8$, $5\pi/8$, $7\pi/8$, $9\pi/8$, $11\pi/8$, $13\pi/8$, and $15\pi/8$, respectively.

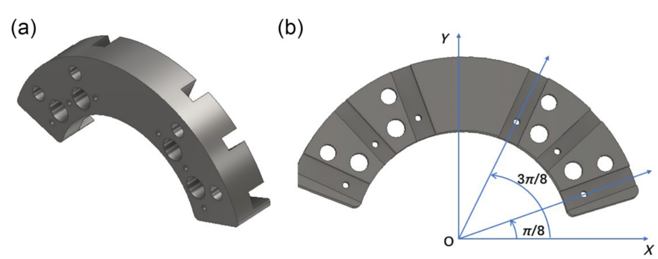

FIG. 8. 3D model (a) and back view (b) of the connecting plate with magic finger slots.

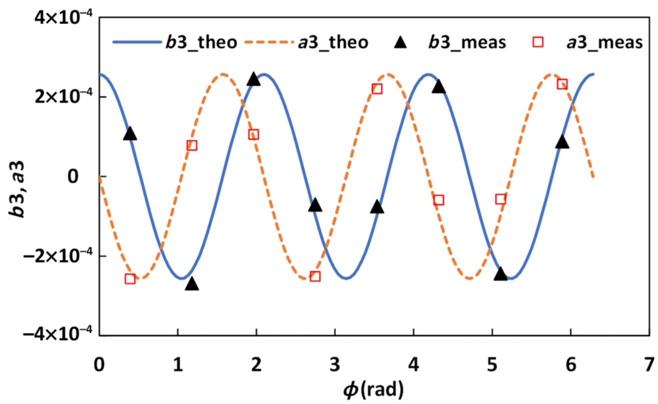

FIG. 9. b_3 and a_3 generated by a magic finger at different positions. The b_3_meas and a_3_meas are the measured variations in the normal and skew sextupole terms caused by a magic finger. The b_3_theo and a_3_theo are the theoretical values that satisfy the formula of $C_3 \cos 3\phi$ and $C_3 \sin 3\phi$.

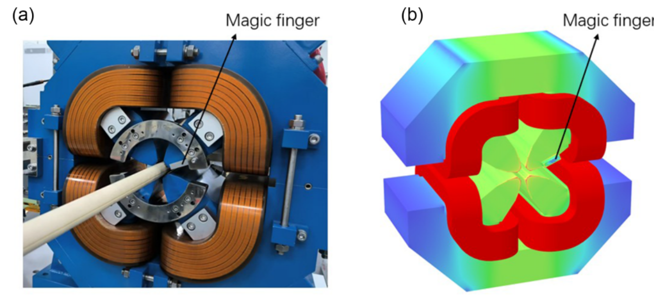

FIG. 10. A magic finger at the angle of $\pi/8$ in QF5 magnet (a) and the 3D model of QF5 (b).

The harmonic adjustment achieved by employing several magic fingers corresponds to the vector superposition of the field components generated by each single magic finger [13].

In a standard type I quadrupole, the variations of normal and skew sextupole components induced by a single magic finger positioned at one of eight locations are plotted in Fig. 9. These variations show a close agreement with the theoretical $C_3 \cos 3\phi$ and $C_3 \sin 3\phi$ curves, where C_3 is the simulated coefficient of sextupole. The measured values deviate from the simulation by 0.3 units. Table III shows the measured harmonics in QD36-43# before and after two magic finger compensations at the $5\pi/8$ and $11\pi/8$.

High-order multipoles (sextupole/octupole) generated by an identical magic finger exhibit a significant variation depending on the quadrupole's length, structural configuration (type I/II), and magnetic saturation levels. Consequently, compensation settings are made according to the actual measurement results of each type and the amount of the field harmonics that need to be adjusted. Figure 10 depicts the magic finger installed within a connecting plate slot in a QF5 quadrupole. To ensure compatibility with vacuum chambers and adjacent components, the finger's profile must not protrude beyond the magnet pole contour. For each quadrupole type, one magnet is selected for the magic finger experiment. The harmonic adjustment components at each angular position are measured to generate a capability lookup table. Subsequently, the magic finger can be used to adjust magnets exhibiting excessive harmonic distortion. This harmonic compensation process typically takes no more than 20 min. The magic finger technology for field harmonic adjustment serves as an auxiliary approach for project schedule adherence and magnet cost reduction.

TABLE III. Harmonics measured before and after magic finger compensation in QD36-43# (1×10^{-4}).

Item	b_3	a_3	b_4	a_4
Before compensation	−6.04	−1.37	0.70	−0.09
After compensation	−2.85	−1.32	0.40	0.01
	Δb_3	Δa_3	Δb_4	Δa_4
Harmonics change	3.19	0.05	−0.30	0.10

III. MECHANICAL DESIGN AND MANUFACTURING PROCESS

Based on the error analysis, the pole profile shape and assembly tolerance for series quadrupoles are set to be smaller than ±0.03 mm for laminated core magnets and ±0.02 mm for solid core magnets [14].

For type I quadrupoles, laminated yokes achieve dimensional accuracy through precision punching, high-tolerance lamination dies, and tight assembly tolerance. A stack of 0.5 mm thick laminations (±0.015 mm tolerance) and DT4 end plates machined by a five-axis CNC are assembled on a mold. Three pretensioned low-carbon steel rods secure each quadrant yoke, which is then subsequently intermittently welded to the outer slots of laminations using three carbon steel backing plates.

The type II quadrupole introduces further complexity in the engineering design of the magnets. Their yokes are made of DT4 electric pure iron. The quadrupole's core consists of an assembly of four yokes and four stainless steel blocks positioned on the horizontal plane. Prior to assembly, the yoke profiles undergo rough machining via CNC. The pole profile of the final assembled structure (length < 300 mm) is fine-machined by slow wire electrical discharge machining (EDM).

Both the end plates in type I and the solid iron in type II are annealed after coarse machining. The solid components were heated to 925 °C, held at this temperature for 3 h, and then cooled to room temperature at a rate of less than 60 °C/h. The primary objectives of this process are to eliminate impurities, soften the material, and reduce coercivity. Following the assembly of the four quadrant

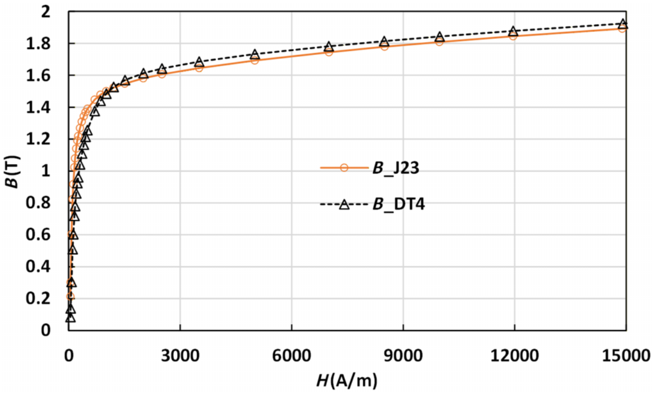

FIG. 11. Measured BH curves of laminations (J23) and solid iron (DT4).

yokes, locating pins are drilled. Subsequently, the iron structure is painted prior to coil assembly.

Figure 11 shows the measured BH curves for the laminations (J23) and the annealed solid iron (DT4). At a field strength of 1000 A/m, the respective magnetic flux densities of the J23 and DT4 are 1.486 T and 1.483 T. These rise to 1.806 T and 1.843 T, respectively, at 10, 000 A/m. Across the multipole samples, the maximum difference in flux density between the laminations is less than 0.036 T. Notably, in the pole region of primary interest to us, where the magnetic field exceeds 1.5 T, the difference between the BH curves of the J23 samples is less than 0.009 T. For the DT4 samples, the maximum difference across the entire excitation range is less than 0.03 T, and above 1.5 T, it is less than 0.02 T.

The exciting coils are constructed from hollow oxygen-free copper conductors. Each coil consists of four layers with seven turns per layer and is equipped with a cooling circuit. As shown in Fig. 12(a), both ends of the pole root are chamfered with a triple line to match the bending radius of the coil package, which reduces the total longitudinal length of the magnet and cuts down the field crosstalk.

For QD36, the electromagnetic force between adjacent poles at the operating current is approximately 5.9 kN.

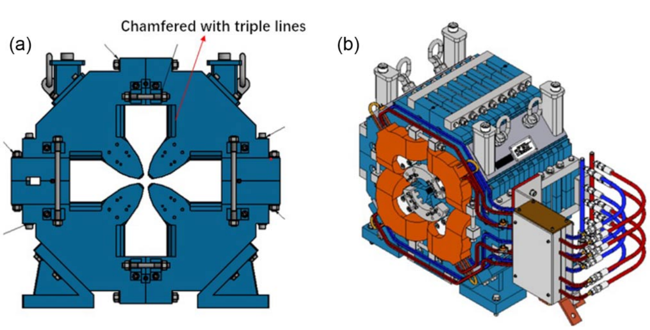

FIG. 12. QD7 iron core model drawing without connecting plates (a) and QD36 assembly drawing (b).

Considering both gravity and magnetic force in finite element analysis simulation, the calculated maximum deformation of the poles is less than 3 μm, which is negligible. The pole connecting plates effectively maintain the positions of the two upper or two lower poles and enhance structural rigidity, as shown in Fig. 12(b). This robust structure ensures excellent mechanical strength and repeatability during reassembly.

Once the dimensional measurements are completed, all mechanical parameters meet the specified requirements, and hydroelectric testing is passed, the magnets are delivered to IHEP.

IV. SPECIAL FEATURES OF SATURATED QUADRUPOLE MAGNETS

A. Clearances between the pulling rods and laminations in laminated quadrupoles

Before large batch production, the initial prototypes of each family are measured and tested. For type I quadrupole prototypes with laminated cores, the integrated gradients at designed operating currents are lower than the specified requirements. Taking QF16-245-01# as an example, to achieve the required integrated gradient, it is necessary to increase the current from the designed value 206 to 223 A. This leads to two issues: a rapid increase in power consumption under saturated conditions and the inability of certain quadrupole types to reach the required integrated gradient due to limitations in the power supply range.

In contrast, for type II quadrupoles with solid iron cores, the measured current needed to reach the nominal integrated gradient is nearly equivalent to the designed value. The primary distinctions between type I and type II quadrupoles reside in their mechanical structures and iron materials. The magnetic properties of laminations and solid iron were evaluated on samples; however, differences observed in BH curves do not sufficiently explain such a significant gradient disparity in laminated quadrupoles. Furthermore, considerations regarding the packing factor of laminated yokes are incorporated into 3D simulations.

Detailed calculations and analyses were performed on the magnet structure. In contrast to solid iron, each quadrant yoke consists of lamination sheets in the middle and solid DT4 plates at both ends. Three pull rods are utilized in each quadrant to compress the laminated sheets and end plates into a cohesive unit. The holes present in the laminated sheet are illustrated in Fig. 13(a). These rods are fabricated from low-carbon steel, ensuring adequate strength for their application. It is essential that the rod positioned on the pole head be located as far from the aperture center as feasible to minimize pole saturation; however, it must remain sufficiently close to guarantee secure fastening of the pole head. In cross-sectional view, the optimal distance from the aperture center is approximately 90 mm.

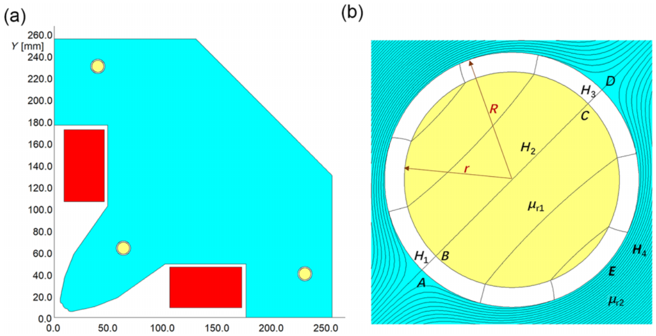

FIG. 13. Layout of three pulling rods in the quadrant (a) and magnetic flux lines around the pulling rod at the pole head (b).

As shown in Fig. 4(a), the magnetic flux density is highest in the pole region, and the clearance between the pull rod and the laminations is a critical parameter. When the field is penetrated into the rod region at the pole, the flux first passes through the gap with a relative vacuum permeability of $\mu_{r0} = 1$, then through the rod region with a relative permeability of μ_{r1}, and finally through the air gap into the laminated region, as illustrated in Fig. 13(b). While the laminations become saturated, the relative permeability μ_{r2} decreases sharply. Following the Ampèere theorem, the rough approximation of the integral field in and outside the hole can be equal. The following relation can be obtained:

$$\int_0^{R-r} H_1 dr + \int_0^{L_{\mathrm{rod}}} H_2 dl + \int_0^{R-r} H_3 dr = \int_0^{C} H_4 dl. \tag{1}$$

In the above equation, $R = 6.5$ mm represents the hole radius in the lamination sheets, r denotes the radius of the pull rod, and C is defined as half of the perimeter of the hole, which corresponds to the shortest path outside of it. L_{rod} indicates the length over which the magnetic flux passes through the pull rod. The variables H_1, H_2, H_3, and H_4 represent the average magnetic intensity along the lines AB, BC, and CD and along the half-circle line AED, respectively. L_{rod} equals $2r$ in the line BC.

We assume that magnetic density remains constant within both the narrow gap regions and rod areas as well as the localized sections of the laminations; this also applies to the relative permeabilities. Given that these fields are consistent throughout, we can approximate $B_{\mathrm{air1}} \approx B_{\mathrm{air2}} \approx B_{\mathrm{rod}}$. Consequently, Eq. (1) can be simplified as follows:

$$2B_{\mathrm{rod}}(R - r) + 2r\frac{B_{\mathrm{rod}}}{\mu_{r1}} = \pi R\frac{B_{\mathrm{sat}}}{\mu_{r2}}. \tag{2}$$

B_{sat} refers to the magnetic field along the line AED surrounding the hole in the laminations. Given that the air region exhibits a higher reluctance compared to the magnetic components (i.e., the rod and laminations), the rod remains significantly less saturated at nominal gradient. According to the BH curve derived from the material sample testing, μ_{r1} is approximately 2700 in the rod when the quadrupole is under nominal gradient. In contrast, within the lamination region adjacent to the hole at the pole root, relative saturated permeability μ_{r2} ranges from 100 to 300. Consequently, it follows that $\mu_{r1} \gg \mu_{r2} \gg \mu_{r0} = 1$. Thus, we get Eq. (3):

$$B_{\mathrm{rod}} = \frac{\pi R}{2\mu_{r2}(R - r + \frac{r}{\mu_{r1}})} B_{\mathrm{sat}}. \tag{3}$$

Equation (3) illustrates that the magnetic flux density B_{rod} in the rod is inversely proportional to the clearance (R-r) between the rod and the laminations. Due to the reduced cross section with a hole in the pole root, the pole saturation here is more pronounced than that without a hole. This results in diminished magnetic efficiency. Figure 14(a) depicts the simulated value of B_{rod} against the clearance (R-r). The simulated results align closely with the trend predicted by Eq. (3), while discrepancies primarily arise from evaluation of the magnetic permeability and approximations concerning average fields across the rod, air gap clearances, and laminations.

$$\int_0^{R1} H dr + \int_0^{L_{\mathrm{iron}}} H dl = NI, \tag{4}$$

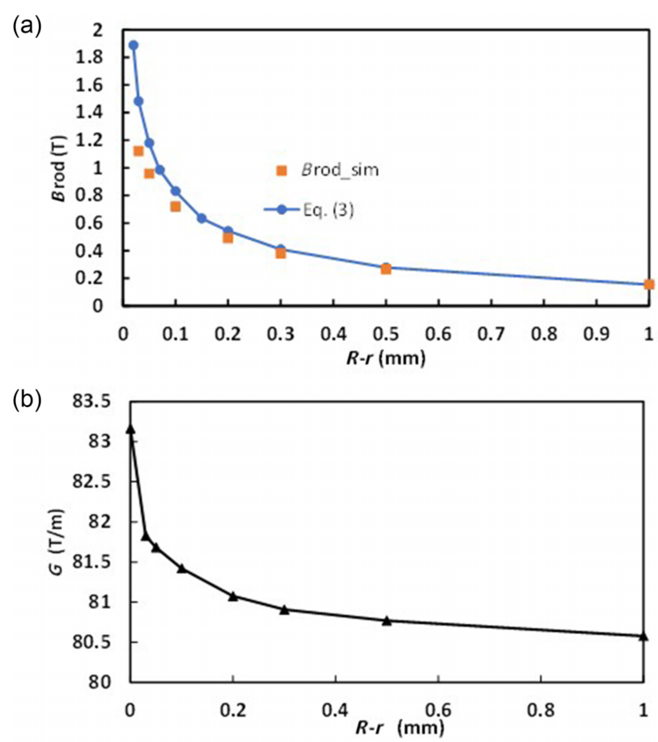

FIG. 14. B_{rod} in the rod region versus clearance between the rod and hole (a) and gradient versus clearance ($R - r$) (b).

$$\frac{G_0 R_1^2}{2\mu_0} = NI - \int_0^{L_{\text{iron}}} H dl. \qquad (5)$$

From the Ampèere theorem, we get Eqs. (4) and (5), in which $R_1 = 13$ mm represents quadrupole aperture radius and G_0 signifies gradient within this aperture; NI indicates total Ampère-turns, where N denotes the turns of the excited coil and I represents the excitation current. Local fields within the hole and nearby iron regions experience disturbances leading to increased reluctance along close flux paths of quadrupoles. With a constant Ampère-turns value, an enhanced magnetic reluctance in the iron region with a hole implies reduced reluctance within the aperture, thereby decreasing the field gradient, as shown in Eq. (5). Figure 14(b) shows the gradient variations versus clearance. 2D simulations reveal a 2.88% gradient reduction at a 0.5 mm rod-lamination clearance, compared to a no-hole pole root configuration.

To facilitate pull rod installation and machining processes, this clearance was reduced from 0.5 mm in prototypes to 0.05 mm in batch production. 2D calculations demonstrate that this modification increases the magnetic induction density within the rod from 0.26 to 0.96 T. However, acting as a flux shunt causes field strength near lamination areas surrounding the hole to decrease from 1.81 to 1.66 T while simultaneously enhancing aperture gradient by 1.3%. This effect may be further pronounced under 3D simulation conditions.

When the quadrupole gradient is reduced to 50% ($\approx$40 T/m), the resulting field strength yields sufficiently high μ_{r2} in the pole, rendering rod-to-lamination clearance noncritical. Neither the gradient nor the simulated B_{rod} (magnetic flux density in the rod) is influenced by variations in clearance or rod position. The simulated B_{rod} remains below 0.05 T across all clearance configurations.

Other aspects, including rod nut size and the material of the rod and bolt nuts, are modified based on finite element calculations. The objective of these modifications is to increase the iron filling ratio (defined as the proportion of iron area in a given cross section) and to mitigate magnetic saturation. Finally, this leads to a reduction in the operating currents required to achieve the target integrated gradient, bringing them close to the designed values.

B. Unexpected sextupole growth in solid quadrupoles induced by core material inhomogeneity

Initial batch field measurements revealed that the sextupole component in solid magnets exceeded the specified limits at the operating current. When investigating its current dependence, laminated magnets demonstrated stable sextupole behavior. However, most solid magnets show a rapid increase in sextupole components beyond a critical current threshold despite moderated core saturation

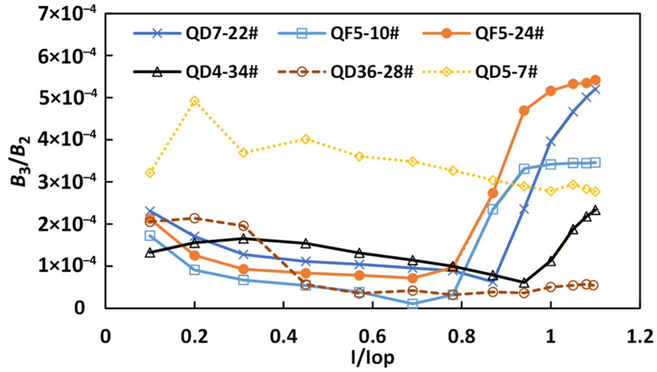

FIG. 15. Measured sextupole component versus current in different quadrupoles. QD7, QF5, and QD4 are solid magnets, and QD36 and QD5 are laminated magnets. Iop is the operating current of each quadrupole.

levels remaining intact. Figure 15 illustrates this current-dependent variation of the sextupole component across different quadrupole types.

Simulation and measurement results indicate the sextupole component is primarily influenced by mechanical errors and inhomogeneity in core material properties. Mechanical errors are largely independent of the current, whereas the material effects exhibit a high sensitivity to iron magnetic saturation. Even at an excitation efficiency of 99%, the contribution from the material significantly affects the sextupole component due to a rapid decline in magnet permeability. Shorter magnets demonstrate higher excitation efficiency at the onset of sextupole growth. For example, QD7, with an iron length of 180 mm, begins its sextupole increase at an excitation efficiency of 99.53%. In contrast, QF5 (201 mm) and QD4 (260 mm) initiate this increase at efficiencies of 98.92% and 98.79%, respectively.

This phenomenon is observed in other magnets, such as in HEPS type I combined dipole and quadrupole magnets with solid iron. However, in type II laminated quadrupoles, the sextupole component remains nearly constant across varying excitation currents. The issue of unexpected sextupole field growth stems not from structural differences between the type I and type II designs but rather from the use of solid iron.

In laminate magnets, the laminated sheets are blended before and after the punching process. The length of the end plates constitutes only a small fraction of the total iron length. Consequently, the four laminated quadrants demonstrate relatively uniform magnetic properties in both longitudinal and transverse directions. Higher-order harmonics are predominantly influenced by mechanical tolerances established during component machining and magnet assembly. As a result, the field harmonics remain nearly constant throughout the ramping process.

Solid quadrupoles can exhibit magnetic inhomogeneity due to material variations within or between the iron blocks used to construct the four quadrants. This inherent

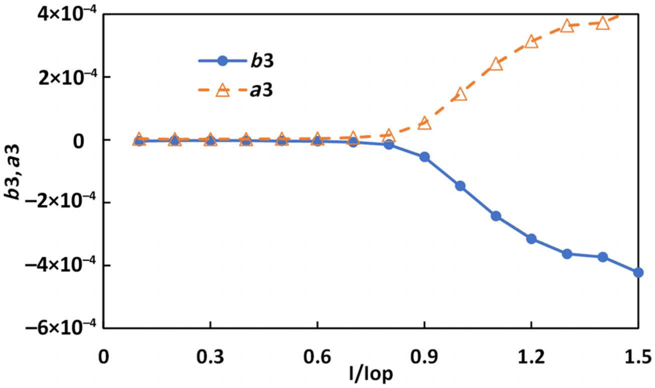

FIG. 16. Simulated sextupole term versus current in QD5 with a 1% lower B value in the BH curve in the first quadrant.

FIG. 17. Quadrupole magnets to be tested in the experimental hall.

mismatch in magnetic properties, particularly under saturation, leads to differing magnetization characteristics across yoke segments. Consequently, the magnetic fourfold symmetry is compromised, thereby generating higher-order field harmonics.

To investigate the observed sextupole behavior, case studies have been conducted using OPERA by manually modeling a slightly different BH curve for one of the iron quadrants. Figure 16 shows the simulated sextupole components with current. A mere 1% reduction in magnetic density in the first quadrant leads to an increase in the sextupole component as saturation begins to occur in the iron. Other forms of material asymmetry or inhomogeneity would similarly affect the trend of sextupole behavior.

The octupole component is hardly affected by material inhomogeneities, as variations in material properties among one or more of the four yokes seldom affect the symmetry of the octupole field. The octupole component arises primarily from mechanical tolerances.

Magic fingers are predominantly employed for compensating magnetic field harmonics in solid quadrupole magnets that do not conform to specifications. Accelerator physics simulations confirm that the magnetic disturbances caused by magic fingers in a small number of magnets have negligible effects on beam dynamics [15].

V. BATCH MAGNETIC FIELD MEASUREMENT RESULTS AND DISCUSSION

A robust magnetic measurement capability is essential for ensuring the field quality of the magnets and addressing various technical challenges. Hall probe field measurements are conducted for integrated gradient calibration and longitudinal magnetic field distribution analysis. For mass production magnets, the assessment of magnetic performance—including multipole components, magnetic center, and excitation curves—depends on rotating coil measurement systems. This selection is motivated by the high reproducibility and efficiency offered by these systems.

After leaving the manufacturing facility, the magnets were transported to the experimental hall for testing and prealignment, as shown in Fig. 17.

The measurement systems are housed in a temperature-controlled laboratory with a temperature of 25 °C ± 0.3 °C. The magnets shall be preconditioned at this constant temperature for at least 12 h prior to testing.

A. Hall probe measurement results

Figure 18 shows a QD5 quadrupole installed on a Hall probe measurement system. The vertical field strength along the longitudinal direction in the horizontal midplane is measured to investigate its field distribution and calculate both the integrated gradient and magnetic length.

The QD5 features a laminated yoke with 30 mm thick DT4 end plates, while QD4 employs solid DT4 iron. Both magnets possess an iron length of 260 mm. Figure 19 presents a comparison of the longitudinal distribution of B_y and its normalized value B_y/B_{yc} for QD5 at currents of 131 A and 190 A (Iop), alongside QD4 at 186 A (Iop). Here, B_{yc} denotes the vertical field component at (5 mm, 0, 0). It is evident that once saturation occurs in the core

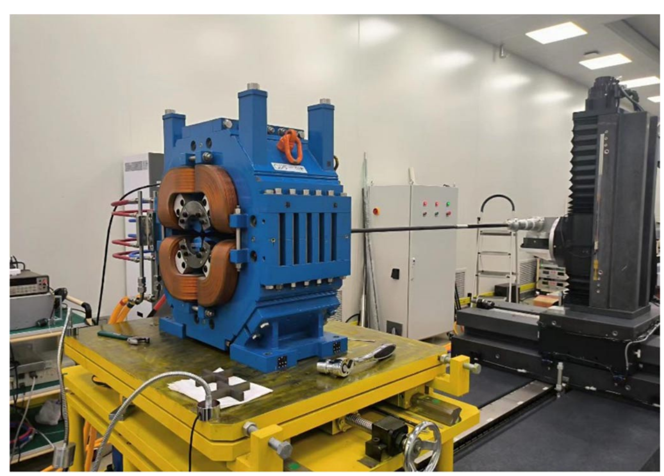

FIG. 18. QD5 installed on a Hall probe measurement system.

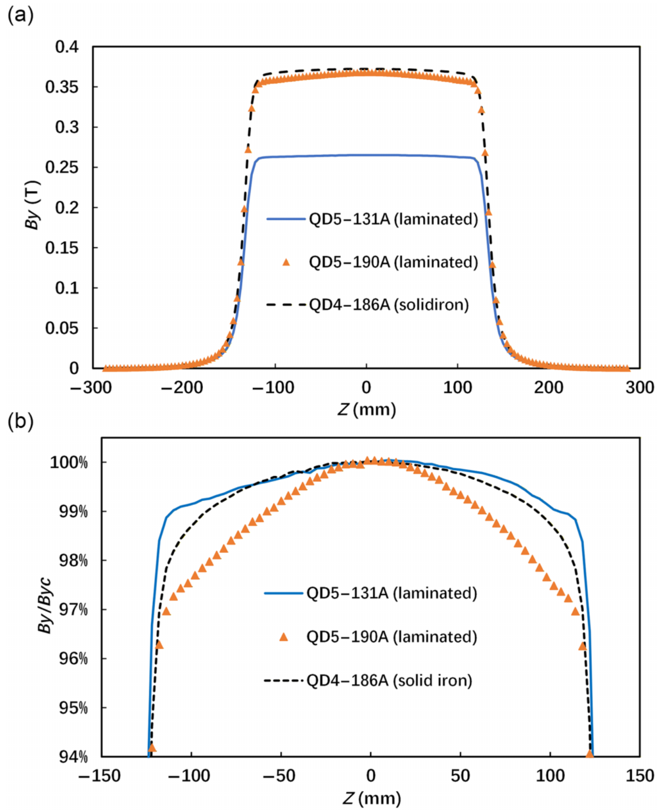

FIG. 19. B_y along z at $x = 5$ mm and $y = 0$ in QD5 and QD4 (a) and relative B_y/B_{yc} at (5,0,0) in QD5 and QD4 (b).

(as observed in QD5 at 190 A), the saturation effect becomes pronounced toward the end of the magnet, resulting in a diminished magnetic field strength. Additionally, there is a notable bump between the laminated irons and end plates in QD5 at an operation current of 131 A, as depicted in Fig. 19(b). The center gradient for QD5 measures 73.87 T/m when operated at 190 A, while it reaches up to 74.62 T/m for QD4 operating at 186 A, indicating that solid magnets yield higher gradients.

This Hall probe measurement system accurately quantifies the integrated gradient of nine different types of magnets, with two to three units sampled per type. All measured integrated gradients satisfy the specified design criteria. The nominal operating current is derived from these measurements and subsequently utilized for the rotating coil measurements.

B. Rotating coil measurement system and magnetic center results

The magnetic characteristics of the batch quadrupoles are evaluated using two rotating coil measurement systems based on coordinated measuring machine (CMM) [16]. The system consists of a servomotor equipped with an accurate encoder at the active end, along with two 2D linear stages on both ends to support the rotating coil. Additionally, it includes a fast digital integrator FDI2056

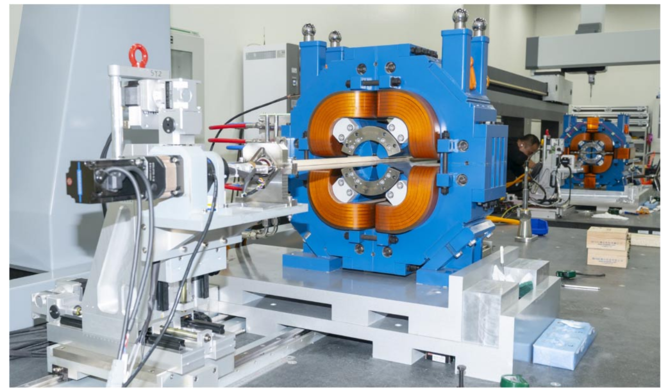

FIG. 20. Quadrupole magnets installed on the rotating coil measurement systems.

[17] for signal acquisition and control devices. As shown in Fig. 20, the quadrupoles are mounted on test benches, while the CMM marble granite platforms serve as the foundation for all equipment.

The rotating coil features a skeleton constructed from Al_2O_3, which offers lightweight properties and high stiffness. With a main coil radius of 11 mm, the field harmonics are expressed at a reference radius of 5 mm. Both main and compensation windings are wound in the precision-machined grooves to effectively cancel out the dipole and quadrupole components [18,19]. During measurement, the rotating coil is inserted into the quadrupole aperture and supported at both ends by V-shaped brackets affixed to linear stages. The orthogonality of the translation stages is calibrated by CMM. The measurement accuracy depends mainly on the winding precision. In-site calibration of the coil radii is computed through field measurements performed before and after translating the coil within the quadrupole aperture [20–22].

The quadrupole's mechanical coordinate system is established using CMM measurements of the eight interpole gaps and the top-mounted target balls, achieving 5 μm accuracy. The mechanical axis of the rotating coil is detected by the CMM with a precision of less than 4 μm and aligned to the quadrupole's mechanical center utilizing two 2D linear stages.

The repeatability of the measurement system was evaluated through multiple measurements. Typical noise levels in harmonic measurements were found to be below 0.3 units (one unit means 10^{-4} of main quadrupole strength). Repeated integrated gradient measurements show high stability with a relative standard deviation of 5×10^{-5}. The standard deviations of the measured magnetic center are less than 5 μm, even after disassembling and reassembling the rotating coil.

Figure 21 illustrates the eight interpole gaps across 98 QD36 quadrupoles. The average value for these gaps is 11.005 mm with a standard deviation of 0.017 mm. The magnetic center x_0 and y_0 are calculated using data from

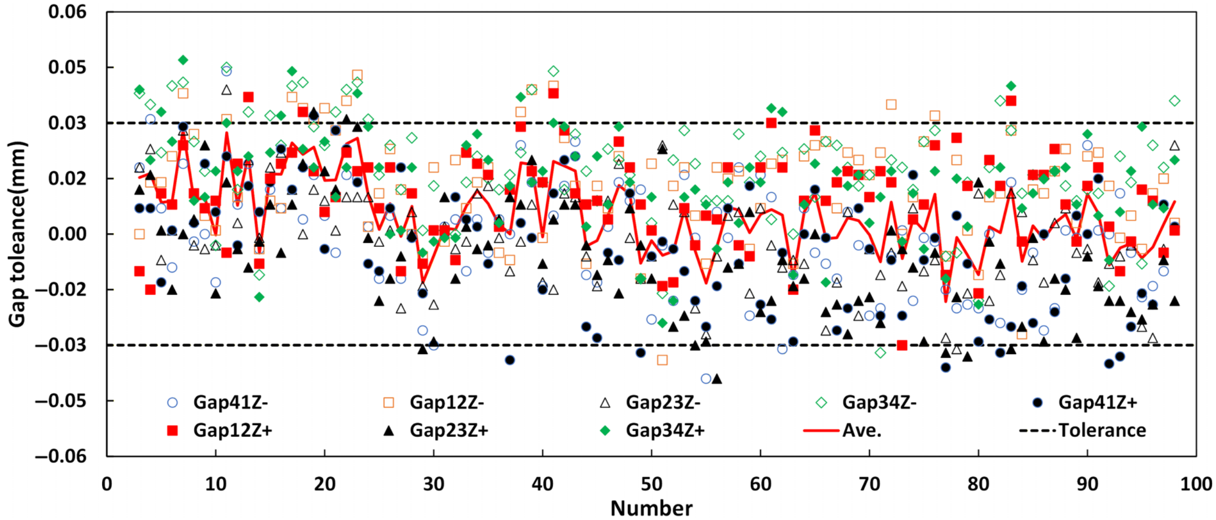

FIG. 21. The gap tolerances between adjacent poles in 98 QD36. The gaps are between the four quadrant yokes at both ends; Gap41Z- indicates the gap between pole 1 and pole 4 at the negative end of the longitudinal direction.

the rotating coil measurement system. Figure 22 presents the magnetic centers of all 98 QD36 units. The mean value for x_0 and y_0 is −3.6 and 1.3 μm, respectively, while their corresponding standard deviations are noted as 9.3 and 11.6 μm, respectively. The magnetic centers have been extracted to align with top targets with a precision of 10 μm, facilitating prealignment in the girder assembly process.

C. Transfer function of quadrupoles

The excitation curves were measured across a sequence of currents using rotating coil measurement systems. The integrated field strength was derived via cubic spline interpolation and subsequently fine-tuned with independent power supplies.

Following three cycles of current from 0 to the maximum current (1.1 Iop) for each magnet type, the integrated gradients were measured at various currents using a rotating coil positioned at the magnetic center. The averaged integral transfer functions (ITF) across nine types of quadrupoles are calculated. To account for minor systematic differences between different types, the ITF values are normalized to 0.2 times the operating currents of each quadrupole type and compared, as plotted in Fig. 23(a).

For magnets with the identical iron lengths, solid magnets achieve a larger integrated gradient and higher excitation efficiency than laminated magnets, despite their operating current being lower than that of laminated magnets. At the operating current, the rms spreads of

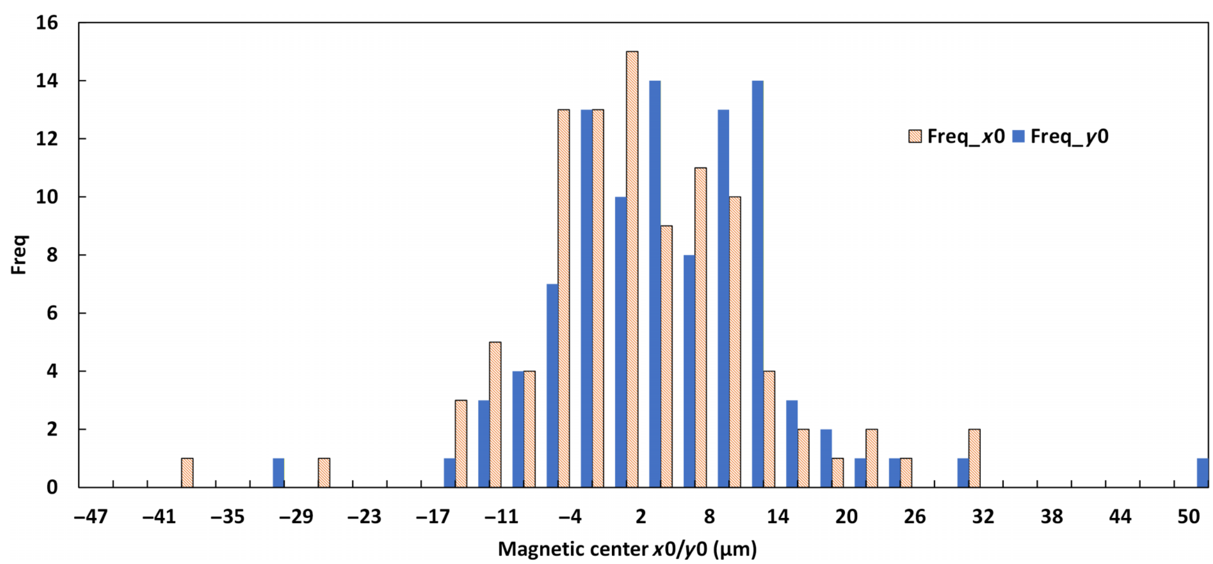

FIG. 22. Statistical distribution of magnetic center in 98 QD36 at nominal current.

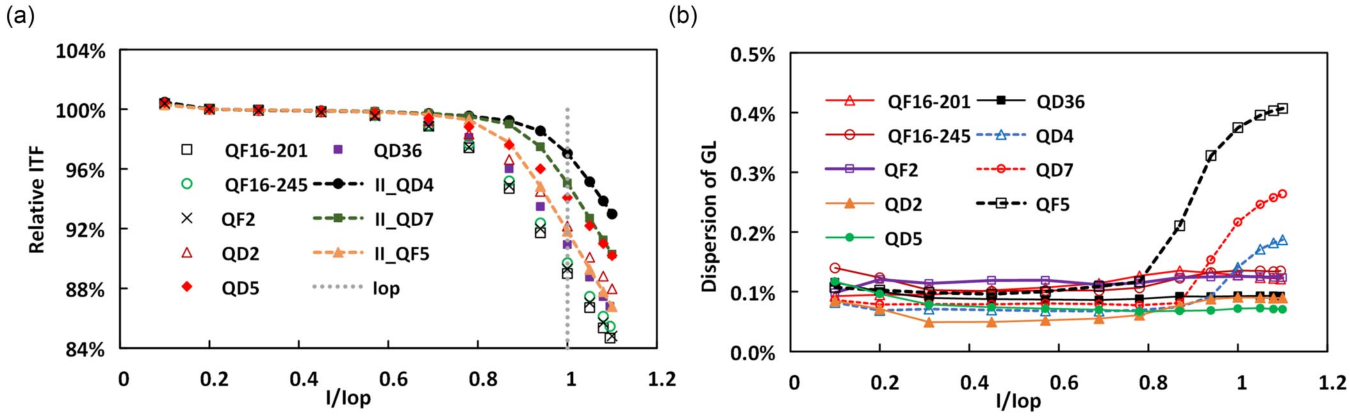

FIG. 23. Relative integrated transfer functions (a) and dispersion of GL (b) across nine types of quadrupoles. GL means integral gradient.

integrated gradients for QD5 and QD4 are 0.071% and 0.14%, respectively. Meanwhile, at 0.69 Iop, the rms spreads for QD5 and QD4 are 0.07% and 0.068%.

Laminated quadrupoles exhibit small dispersion in integrated gradients that is independent of current; conversely, solid quadrupoles demonstrate an increasing dispersion with rising current, as shown in Fig. 23(b). This behavior stems primarily from amplified material-dependent effects in iron cores under saturation conditions.

D. Multipole components of batch quadrupole magnets

Several aspects of magnet performance have been thoroughly analyzed. The normal and skew components as a function of current are plotted in Fig. 24. Besides the allowed multipole fields, the primary measured harmonic components in the quadrupoles are the sextupole and octupole components. As previously mentioned, the sextupole component in laminated quadrupoles remains constant at various currents, while it increases sharply in solid

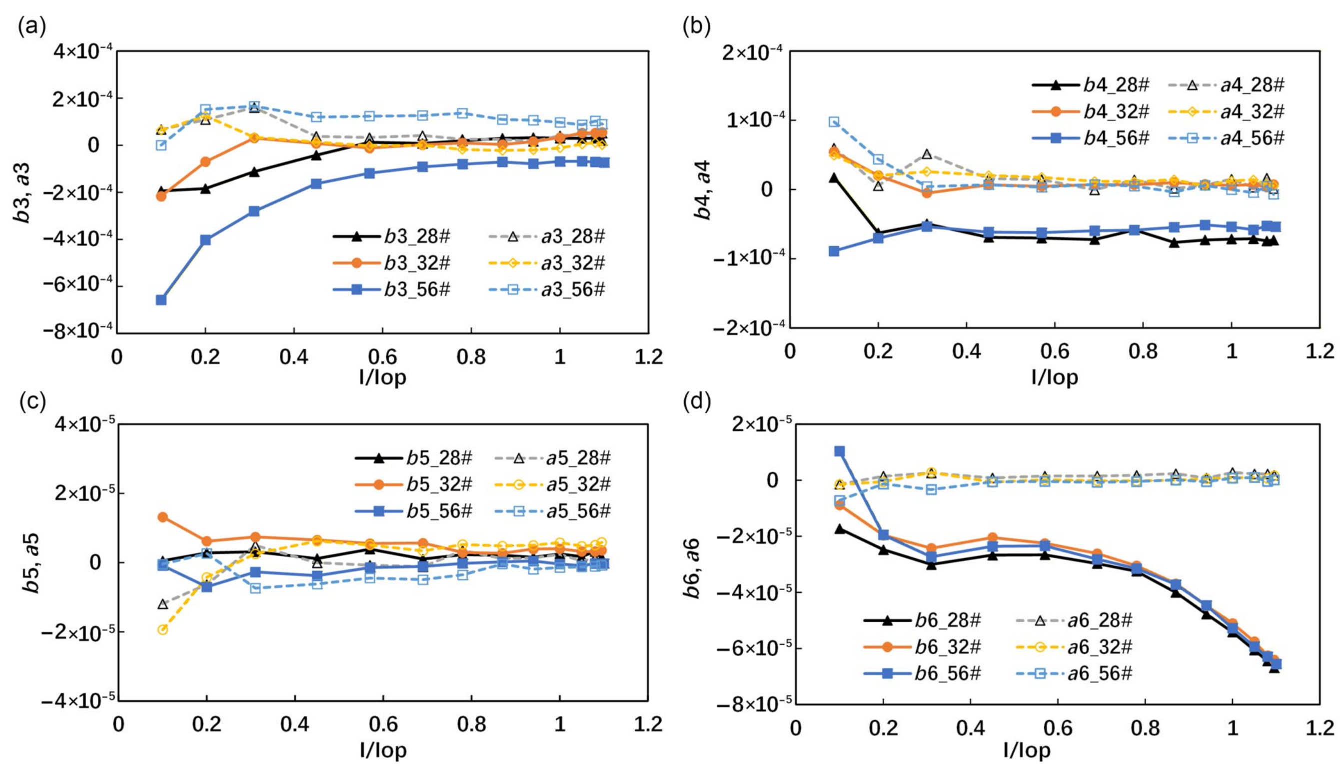

FIG. 24. Measured normal and skew components as a function of current in three QD36. Iop = 214 A. (a) b_3 and a_3, (b) b_4 and a_4, (c) b_5 and a_5, and (d) b_6 and a_6.

quadrupoles. Other multipole components exhibit similar trends in both the laminated and solid quadrupoles. Nearly constant values for the octupole and decapole components are observed across different currents, as shown in Figs. 24(b) and 24(c) in three QD36. Furthermore, Fig. 24(d) indicates that the amplitude of normal dodecapole (b_6) increases as the magnets approach saturation, which is consistent with the simulated results in Opera/3D. Within the operational range of all QD36 units, harmonics meet specified requirements effectively. The values of the other harmonic components remain low, less than 0.2 units, which is comparable to the accuracy of the measurement system and can be disregarded.

A few overtolerance magnets are compensated by magic fingers. Consequently, the field performance of all 480 quadrupoles meets the physical specifications. Table IV presents statistics on multipole component distributions in three types of quadrupoles. Field errors are predominantly influenced by sextupole components: both normal and skew sextupole terms exhibit a standard deviation of about 1.5 units, whereas for the normal octupole component, this standard deviation is only 0.3 units. The average b_6 across these three types of quadrupoles is about 0.5 units, determined by pole profile design, integrated gradient, and end effects. Other higher-order harmonics maintain significantly small amplitudes throughout their ranges; moreover, harmonic dispersion decreases monotonically with increasing harmonic order.

The averaged values of b_4 for all three types of quadrupoles exhibited a positive bias, which can be attributed to the asymmetric tolerance distributions observed during magnet assembly. A statistical analysis of adjacent pole gaps revealed systematic deviations: the up and down gap tolerances were found to be positive, while the left and right tolerances both averaged close to zero. This mechanical asymmetry consistently resulted in positive b_4 values, aligning with simulation predictions. These findings demonstrate that octupole components are primarily influenced by mechanical tolerance rather than being dependent on material properties.

TABLE IV. Main meteorological characteristics of the average values and standard deviations for each harmonic of the batch quadrupoles QD5, QD4, and QD36 under operating current (units).

	48 QD5		48 QD4		98 QD36	
Item	Ave.	St. dev	Ave.	St. dev	Ave.	St. dev
b_3	0.22	1.26	0.07	1.32	0.10	1.46
a_3	0.09	1.45	0.64	1.73	−0.53	1.26
b_4	0.38	0.31	0.52	0.30	0.62	0.34
a_4	0.06	0.09	0.07	0.10	0.03	0.12
b_5	−0.02	0.05	0.00	0.05	−0.04	0.07
a_5	−0.03	0.06	−0.01	0.06	−0.01	0.06
b_6	−0.55	0.03	−0.43	0.04	−0.55	0.02
a_6	−0.01	0.01	−0.02	0.03	−0.01	0.01

VI. CONCLUSIONS

This article presents a comprehensive overview of the design, manufacturing, and batch testing of small aperture, high gradient quadrupole magnets for HEPS storage ring. These quadrupoles feature a compact cross section with an optimized pole profile that increases the interpole gaps to 11 mm. By employing saddle coils and tapered poles, they achieve high iron filling ratios, effectively mitigating core saturation and enhancing excitation efficiency. Strict mechanical tolerances (±0.02 mm for solid magnets and ±0.03 mm for laminated magnets) are maintained to ensure magnetic field quality. As a result of these meticulous efforts, magnet production was successfully completed, with all quadrupoles meeting the specified requirements.

Extensive studies have been undertaken to address the saturation issues inherent in high gradient quadrupoles. The saturation renders the magnetic field more sensitive to variations in the iron core, such as clearances between pull rods and holes in the laminations, which ultimately diminish magnetic excitation efficiency. The material discrepancies among the four solid quadrant yokes introduce a significant sextupole component that increases sharply as the iron gets saturated. At a low or moderate field strength, the mechanical tolerances play a predominant role, whereas at high fields, material consistency within the four iron quadrants becomes critical as permeability decreases substantially.

Statistical characteristics were analyzed based on batch field measurement results, confirming the feasibility of both solid and laminated iron structures for high gradient quadrupoles. Solid quadrupoles exhibit higher excitation efficiency; however, they necessitate stringent uniformity of magnetic materials across the four quadrant yokes. In contrast, laminated quadrupoles provide consistent integrated gradients and excellent field quality.

Following installation of these 480 pure quadrupoles in the HEPS tunnel, the High Energy Photon Source successfully delivered its first synchrotron light on October 12, 2024, marking a significant transition to the beam-commissioning phase.

ACKNOWLEDGMENTS

This work is supported by High Energy Photon Source (HEPS), a major national science and technology infrastructure project in China.

DATA AVAILABILITY

There are no publicly available research data or software supporting this manuscript. Requests for further information or data should be sent to the authors.

[1] Y. Jiao, G. Xu, X. Cui *et al.*, The HEPS project, J. Synchrotron Radiat. **25**, 1611 (2018).

[2] Y. Jiao, F. Chen, P. He, C. Li, J. Li, Q. Qin, H. Qu, J. Wan, J. Wang, and G. Xu, Modification and optimization of the storage ring lattice of the high energy photon source, Radiat. Detect. Technol. Methods **4**, 415 (2020).

[3] Q. Li, F. Chen, C. Li, and M. Li, Design of the longitudinal-gradient dipole magnets for HEPS, Radiat. Detect. Technol. Methods **5**, 1 (2021).

[4] M. Yang, C. Fusan, Y. Xu, Y. Wu, Y. Zhu, Z. Zhang, and B. Yin, Design and field performance of octupole magnet with skew quadrupole component in HEPS, IEEE Trans. Appl. Supercond. **32**, 1 (2022).

[5] G. Le Bec, J. Chavanne, F. Villar, C. Benabderrahmane, S. Liuzzo, J.-F. Bouteille, L. Goirand, L. Farvacque, J.-C. Biasci, and P. Raimondi, Magnets for the ESRF diffraction limited light source project, IEEE Trans. Appl. Supercond. **26**, 1 (2016).

[6] M. Abliz, M. Jaski, A. Jain, M. Borland, G. Decker, and J. Kerby, Magnetic crosstalk simulation between Q2 and L bend magnets of APS-U, Nucl. Instrum. Methods Phys. Res., Sect. A **913**, 48 (2019).

[7] M. Johansson, B. Anderberg, and L.-J. Lindgren, Magnet design for a low-emittance storage ring, Synchrotron Radiat. **21**, 884 (2014).

[8] Y. S. Zhu, F. S. Chen, M. Yang *et al.*, Development of prototype high gradient small aperture quadrupole magnets for HEPS-TF, IEEE Trans. Appl. Supercond. **28**, 4000205 (2018).

[9] N. Li, Y. Y. Guo, Y. Jiao *et al.*, Modelling of the magnetic cross-talk effect of the HEPS storage ring, Nucl. Instrum. Methods Phys. Res., Sect. A **1089**, 171604 (2026).

[10] M. Yang, W. Kang, C. Deng, X. Sun, L. Li, X. Wu, L. Gong, D. Cheng, Y. Zhu, and F. Chen, Magnetic fringe field interference between the quadrupole and corrector magnets in the CSNS/RCS, Nucl. Instrum. Methods Phys. Res. **847**, 29 (2017).

[11] Opera simulation software (2020), https://www.3ds.com/products-services/simulia/products/opera/.

[12] Y. S. Zhu, F. S. Chen, and L. Wu, Multipole magnets and their magnetic field harmonics compensation method, China Patent No. ZL 2017106131363 (2019).

[13] M. Yang, F.-S. Chen, Y.-F. Wu, Z. Zhang, B.-G. Yin, B. Na, and Z.-J. Zhang, Development of short prototype of dual aperture quadrupole magnet for CEPC ring, Nucl. Sci. Tech. **34**, 103 (2023).

[14] N. B. Song, Process review report of type I quadrupole magnets for HEPS storage ring, Internal Report, 2021.

[15] N. Li, D. H. Ji, and Y. Jiao, The influence of magic fingers in quadrupoles on beam dynamics, Internal Report, 2023.

[16] M. Yang, F. Chen, B. Yin, R. Liang, S. Li, and Y. Zhu, A rotating coil measurement system based on CMM for high-gradient small-aperture quadrupole in HEPS-TF, Radiat. Detect. Technol. Methods **5**, 8 (2021).

[17] Fast Digital Integrator FDI 2056, https://www.metrolab.com/products/fast-digital-integrator-fdi2056.

[18] J. Tanabe, *Iron Dominated Electromagnets: Design, Fabrication, Assembly and Measurements* (World Scientific Publishing Co. Pte. Ltd,, Singapore, 2005).

[19] J. K. Animesh, Measurements of field quality using harmonic coils, US Particle Accelerator School on Superconducting Accelerator Magnets, 2001, Houston, Texas, USA.

[20] P. Arpaia, M. Buzio, G. Golluccio and L. Walckiers, In situ calibration of rotating sensor coils for magnet testing, Rev. Sci. Instrum. **83**, 013306 (2012).

[21] P. Arpaia, O. Koster, G. Severino *et al.*, Calibrating the sensing-coil radius by feed-down from a harmonic reference, Report No. CERN-ACC-2015-0073, 2014.

[22] M. Buzio, Magnetic measurement of small aperture quadrupoles at CERN, PSI, Villigen, 2010.